



## Microstructure and properties of Al-coating on AZ31 magnesium alloy prepared by pack-cementation

Jian-jun HU<sup>1,2</sup>, Jing LIAO<sup>1</sup>, Xian YANG<sup>1</sup>, Jing ZENG<sup>1</sup>, Hui LI<sup>1</sup>, Bo SONG<sup>3</sup>, Hong-bin XU<sup>2</sup>, Ning GUO<sup>3</sup>, Yan JIN<sup>2</sup>

1. College of Materials Science and Engineering, Chongqing University of Technology, Chongqing 400054, China;

2. Key laboratory of Advanced Manufacturing Technology for Automobile Parts, Ministry of Education, Chongqing 400054, China;

3. School of Materials and Energy, Southwest University, Chongqing 400715, China

Received 1 February 2021; accepted 15 September 2021

**Abstract:** Al-containing coatings were prepared on AZ31 magnesium alloy by pack-cementation technology. X-ray diffraction (XRD), backscattered electron imaging (BSEI) and energy dispersive spectroscopy (EDS) were jointly employed to characterize the phases, microstructure and composition of the coated samples. The results show that the feedstock composition has a significant impact on the phases, microstructure and thickness of the coatings. For the sample with  $\text{AlCl}_3$  powder as the activator, the coating is very thick and composed of gradient phases and structures from surface to inside, including small amount of  $\beta\text{-Mg}_2\text{Al}_3$ , coarse eutectic-like structure of  $\gamma\text{-Mg}_{17}\text{Al}_{12} + \delta\text{-Mg}$ , and fine  $\gamma\text{-Mg}_{17}\text{Al}_{12}$  precipitations. In contrast, for the sample with  $\text{AlCl}_3$  and pure Al composite powders as the activator, the coating is relatively thin and contains a thin  $\text{Al}_2\text{O}_3$  layer and a small amount of fine  $\gamma\text{-Mg}_{17}\text{Al}_{12}$  precipitates. For the pack-cementation aluminizing that is not protected by high-vacuum or inert gas, the addition of pure Al powders can easily introduce the  $\text{Al}_2\text{O}_3$  layer into the coating to prevent active Al ions further penetrating into the magnesium matrix, resulting in the thin Al-containing coating. The microhardness and corrosion behavior of the two kinds of aluminized coatings were also studied and discussed.

**Key words:** AZ31 magnesium alloy; Al-coating; pack-cementation; surface aluminizing; corrosion resistance

### 1 Introduction

Magnesium alloys have broad application prospects in the fields of aviation, aerospace and transportation due to their excellent comprehensive properties, such as high specific strength [1], large elastic modulus [2], good heat dissipation [3], good shock suppression [4], and high impact load bearing capacity [5,6]. However, the poor corrosion resistance of magnesium alloys is one of the technical bottlenecks restricting their promotion and application [1,7]. In addition to surface alloying [8] or surface structure adjustment [9], surface coating is also considered to be a simple, effective and

economical method that can greatly improve the corrosion resistance of magnesium alloys. Many coating technologies, such as physical/chemical vapor deposition [10,11], plasma electrolytic oxidation [12,13], surface laser cladding [14], and thermal spraying [15], have been widely studied to introduce coatings/films on the surface of magnesium alloys in order to improve their corrosion resistance.

Pack-cementation is one of the most important low-cost methods for preparing thermal diffusion coating on metallic materials [16–18]. Generally, the coating deposited by pack-cementation is metallurgically bonded with the substrate and has strong adhesion [19]. ZHU and SONG [20] used Al

powder as the diffusion source and prepared an Al-rich coating on the AZ91D substrate to successfully improve its corrosion resistance and hardness. LU et al [21] reported that the Al-rich intermetallic coating is composed of  $Mg_{17}Al_{12}$  phase and  $\alpha$ -Mg phase when the pack-cementation temperature reaches 430 °C. The  $Mg_{17}Al_{12}$  ( $\gamma$ -phase) is a common intermetallic compound in the thermal diffusion Al-coating of magnesium alloy [22]. The large volume fraction of  $\gamma$ -phase can not only increase the hardness, but also improve the corrosion resistance of the magnesium alloy. This is because the  $\gamma$ -phase can act as an anode barrier to inhibit the overall corrosion of the magnesium alloy. However, the major challenge of the pack-cementation diffusion coating on metallic materials is to reduce the processing temperature to alleviate or even avoid the coarsen effect on the microstructure and properties of the substrate [23].

It has been reported that the use of molten chloride ( $AlCl_3$  and  $NaCl$ ) as diffusion activator can effectively reduce the diffusion temperature, and can prepare Al-rich coatings on Mg alloys at lower temperatures [24,25]. In this study, two kinds of packed powders were used to prepare the Al-rich coatings on the AZ31 alloy by the pack-cementation technology. The influence of the composition of the packed powders on the microstructure and performance of the Al-coating was studied through carefully microstructural characterization, hardness and potentiodynamic polarization tests.

## 2 Experimental

### 2.1 Sample preparation

AZ31 hot-rolled sheet with a chemical composition of 3.05% Al, 1.05% Zn, 0.42% Mn, 0.04% Si, 0.01% Cu, 0.003% Fe, 0.001% Ni (mass fraction), and Mg in balance was selected as the substrate material. Rectangular specimens with the gauge dimensions of 15 mm × 20 mm × 7 mm were cut from the sheet by wire-cutting. Prior to the pack-cementation aluminizing, the specimens were ground by SiC papers to 48  $\mu$ m, and then ultrasonically cleaned in acetone solution.

Two types of packed powders were used to prepare the coatings on the AZ31 specimens. The coated samples were named as PA-1 and PA-2 according to their different packed powders. The powder composition of PA-1 sample was 50%

$AlCl_3$  (mass fraction, and hereafter) as Al feedstock, 50%  $NaCl$  as activator, while the powder composition of PA-2 sample was 33%  $AlCl_3$  and 33% pure Al as feedstock, and 34%  $NaCl$  as activator. The diameter of all the powders was less than 75  $\mu$ m. Prior to aluminizing treatment, the mixed powders were thoroughly stirred and put into a ceramic crucible, and then sealed with the mixture of refractory and sodium silicate. The aluminizing treatment of both PA-1 and PA-2 samples was performed in a box-type heating furnace at 400 °C for 8 h. After the pack-cementation treatment, the samples were cooled to room temperature in the furnace.

### 2.2 Characterization

The surface phase analysis of the coated samples was carried out by using an X-ray diffraction instrument (XRD, Empyrean Series 2, PANalytical, Almelo, The Netherlands) with  $Cu K_{\alpha}$  radiation. The scanning range was 20°–90°, with an increment of 0.013° per step. Secondary electron imaging (SEI) and backscattered electron imaging (BSEI) detectors installed on a field emission gun scanning electron microscope (FEGSEM, Zeiss Sigma HD, Zeiss, Dresden, Germany) were used to characterize the microstructure from the cross-sectional view of the coated samples. The distribution of each element in the coating was analyzed by an energy-dispersive spectroscopy (EDS, AZtech Max2, Oxford Instruments, London, UK) installed on the FEGSEM. Prior to the microstructure characterization, the samples were ground by SiC papers to 48  $\mu$ m and then corroded with magnesium alloy etching solution (mixing equal amounts of ethanol, glacial acetic acid and deionized water, and then adding picric acid until saturated).

Potentiodynamic polarization test was performed on a Gamry instrument (reference 3000, PA Warminster, USA). The experimental conditions were as follows: room temperature, 1  $cm^2$  of the sample surface as the working area, and 3.5%  $NaCl$  aqueous solution as the corrosive solution. The reference electrode was a saturated calomel electrode, the auxiliary electrode was a platinum electrode, and the working electrode was the samples. The dynamic potential range was from –1.8 to –1.0 V, and the scan rate was 2 mV/s. The microhardness of the sample section was

determined by the automatic location table digital microhardness tester (HVS-1000Z, Shanghai CSOIF Co., Ltd., China) with a load of 0.5 N and a holding time of 10 s.

### 3 Results and discussion

#### 3.1 Phase composition and element distribution of coating

Figure 1 shows the XRD patterns of the uncoated and coated samples. The phases were determined based on the International Diffraction Data Center (ICDD) database. After aluminizing treatment, the intensity of the diffraction peaks of Mg substrate is significantly reduced compared with that of the as-received sample, and the second phases are detected in the coated samples of PA-1 and PA-2. The  $\text{Mg}_{17}\text{Al}_{12}$  phase is observed both in the PA-1 and PA-2 samples. The difference is that there is a small amount of  $\text{Mg}_2\text{Al}_3$  phase existing in the PA-1 sample.

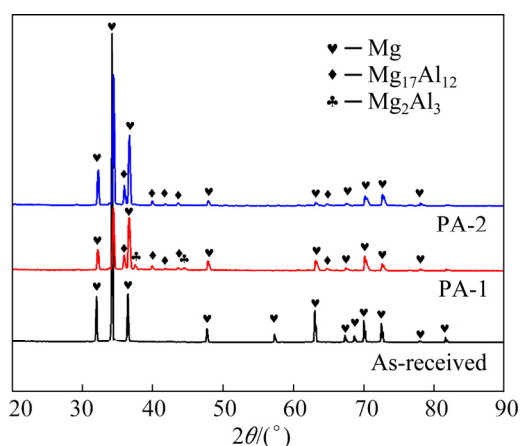


Fig. 1 XRD patterns of various samples

During the pack-cementation processing, permeation and formation of coating are purely due to the diffusion and transfer of atoms and/or ions, which is caused by the difference in the stability of the concentration maintained on both sides of the packed powders and the matrix. As the temperature rises, the concentration of active Al atoms and ions in the packed powders continues to increase and becomes unstable, which causes Al atoms/ions to diffuse to the side of the Mg substrate, and vice versa [24]. According to the Al–Mg binary phase diagram [22], when the Al concentration exceeds its solid solubility in Mg, the  $\gamma\text{-Mg}_{17}\text{Al}_{12}$  will first form, and when the Al concentration continues to increase,

the  $\beta\text{-Mg}_2\text{Al}_3$  phase will form. During the pack-cementation processing, the Al concentration gradually decreases from the outside to the inside, so the  $\beta\text{-Mg}_2\text{Al}_3$  with higher Al content in the coating is closer to the outer layer, while the  $\gamma\text{-Mg}_{17}\text{Al}_{12}$  with relatively low Al content is closer to the Mg substrate. In addition, it can also be inferred that the absence of  $\text{Mg}_2\text{Al}_3$  in the PA-2 sample is because the Al concentration is insufficient in the Al-coating, that is, the diffusion flux is not sufficient in the PA-2 sample during the pack-cementation.

Figure 2 displays the microstructure and EDS results of the two kinds of coated samples. From Fig. 2(a), it can be seen that an Al-coating with a thickness of 180  $\mu\text{m}$  was prepared on the PA-1 sample. The coating thickness is uneven and the coating surface is rugged. Moreover, coarse second phases can be clearly seen in the coating. Unlike the PA-1 sample, as shown in Fig. 2(b), a uniform Al-coating with a thickness of only 25  $\mu\text{m}$  was fabricated on the PA-2 sample. Moreover, the coating of the PA-2 sample is much flatter than that of the PA-1 sample, and no obvious second phases are observed on the coating. The mass fraction ratio of the penetrating element to the matrix element can be used to reflect the reaction of the elements between the penetrating agent and the matrix, that is, whether the coating is composed of a solid solution or a compound [26,27]. Figures 2(c) and (d) show the mass fraction ratio of Al/Mg along the scanning line in the PA-1 and PA-2 samples, respectively. Obviously, the mass fraction ratio of Al/Mg of the former is zigzag, while the latter is linear, indicating that the former is dominated by Al–Mg compounds, while the latter is Al–Mg solid solution (Al–Mg SS). From the above comparison, it can be seen that although the Al element has penetrated into the magnesium matrix, the penetration depth and the interaction with the magnesium matrix are completely different due to the difference of the penetrating agents.

#### 3.2 Microstructure of coating

Figure 3 presents the highly-magnified microstructure and EDS results of the PA-1 sample. Coarse eutectic-like structure can be clearly observed on the outmost surface of the coating, as shown in Fig. 3(a). The coarse eutectic-like structure composed of alternating bright region (P1)

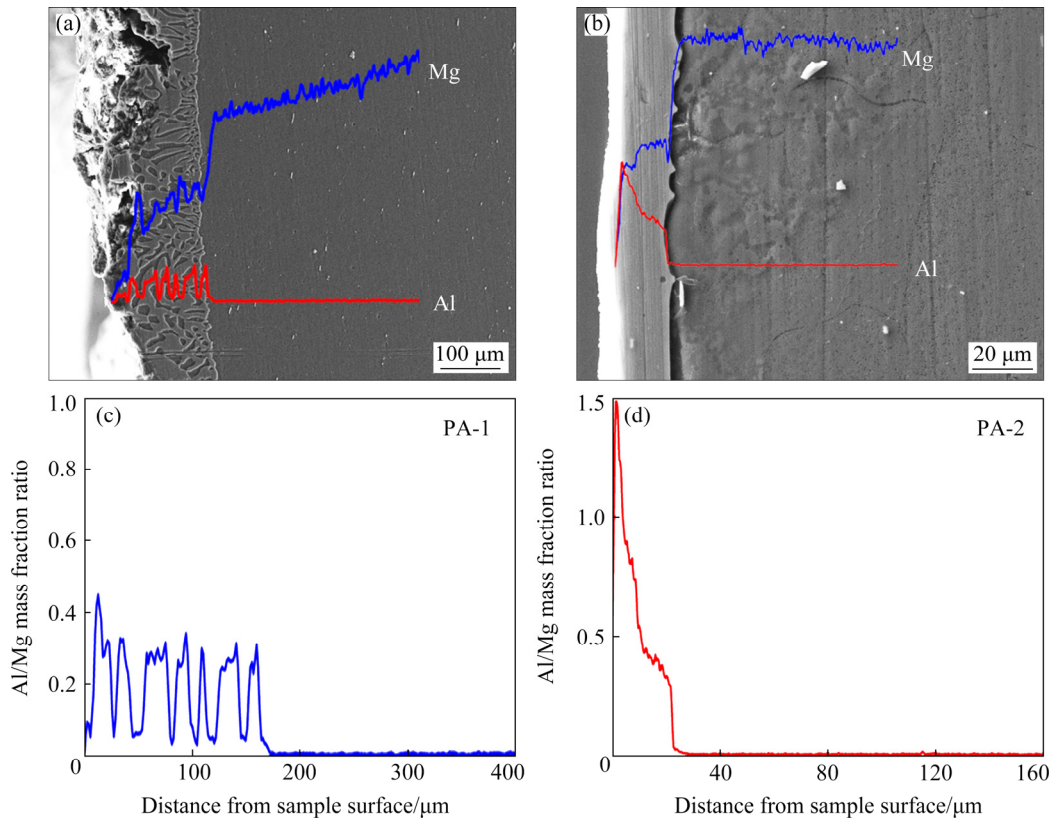


**Fig. 2** SEM images and EDS line scanning spectra (a, b), and Al/Mg mass fraction ratio along depth direction (c, d) of PA-1 sample (a, c) and PA-2 sample (b, d)

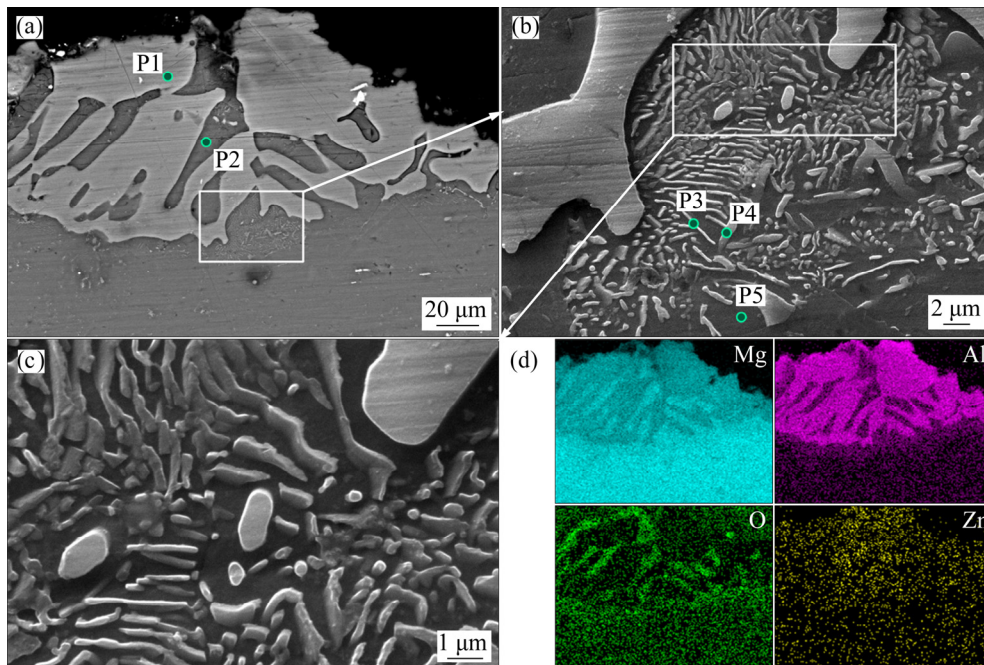


**Fig. 3** Microstructures and element distribution of PA-1 sample: (a, b, c) BSEI image; (d) EDS map

and dark region (P2) can be clearly identified. The EDS maps also confirm that the bright regions are Al-rich phase (see Fig. 3(d)). As shown in Table 1, the EDS results show that the P1 contains more Al

than the P2, respectively corresponding to the  $\gamma$ -Mg<sub>17</sub>Al<sub>12</sub> and  $\delta$ -Mg phases according to the Al–Mg binary phase diagram [22]. That is, the coarse eutectic-like structure is  $\gamma$ -Mg<sub>17</sub>Al<sub>12</sub> +  $\delta$ -Mg.

Figures 3(b) and (c) show the high-magnification microstructure of the layer close to the Mg-substrate. Fine eutectic-like structure also consisting of alternating bright region (P3 and P4) and dark region (P5) can be observed. According to the molar fraction (Table 1) and the binary phase diagram of Al–Mg, P3 and P4 are considered as  $\gamma$ -Mg<sub>17</sub>Al<sub>12</sub>, while P5 is  $\delta$ -Mg. The fine sized  $\gamma$ -Mg<sub>17</sub>Al<sub>12</sub> is considered to precipitate from the  $\delta$ -Mg during cooling after the pack-cementation treatment. This fine Mg<sub>17</sub>Al<sub>12</sub> is considered to have no negative impact on the mechanical properties of the alloys [24]. The microstructure observation once again proves that as the Al concentration gradually decreases from the surface to the inside of the coating, two kinds of eutectic-like structures with different morphologies are formed in the coating of the PA-1 sample: the outer coarse eutectic-like structure of  $\gamma$ -Mg<sub>17</sub>Al<sub>12</sub> +  $\delta$ -Mg and the inner fine  $\gamma$ -Mg<sub>17</sub>Al<sub>12</sub> precipitates on the  $\delta$ -Mg matrix. It should be noted that the  $\beta$ -Mg<sub>2</sub>Al<sub>3</sub> is not directly observed in the microstructure of the PA-1 sample. This may be due to its small amount and small size. Additionally, since the  $\beta$ -Mg<sub>2</sub>Al<sub>3</sub> phase is distributed in the outermost layer of the coating, it cannot be ruled out that the  $\beta$ -Mg<sub>2</sub>Al<sub>3</sub> phase may fall off during the metallographic sample preparation.

**Table 1** EDS analysis results at Points P1–P5 in Fig. 3

Point	Mass fraction/%		Molar fraction/%	
	Mg	Al	Mg	Al
P1	57.82	42.18	60.34	39.66
P2	88.18	11.82	89.23	10.77
P3	82.48	17.52	83.94	16.06
P4	83.90	16.10	85.26	14.74
P5	95.33	4.67	95.77	4.23

Figure 4 shows the microstructure and element distribution of the PA-2 sample. Consistent with the XRD results, the second phase in the coating is very small and almost unobservable, as shown in Fig. 4(a). As discussed above in Fig. 2(b), the coating of PA-2 sample is mainly composed of Al–Mg SS ( $\delta$ -Mg) and a small amount of Mg<sub>17</sub>Al<sub>12</sub>. Clearly, a slight Zn-rich Al-coating can be identified. Because Zn is nobler than Al and Mg, it remains virtually unaffected and therefore enriches on the surface [24]. The EDS point analysis results are

shown in Table 2. It can be seen that with the increase of the diffusion depth from R1 to R3, the concentration of Al decreases and that of Mg increases. Moreover, the outermost layer of the Al coating is oxidized to form a thin aluminum oxide layer. For the PA-2 sample, pure Al powders were added as the feedstock to the packed powders. During the aluminizing treatment, the pure Al powder can directly react with O to form Al<sub>2</sub>O<sub>3</sub>, and the Al<sub>2</sub>O<sub>3</sub> is concentrated in the outermost layer of the coating. It should be noted that the Al<sub>2</sub>O<sub>3</sub> layer is too thin to be identified by the XRD. It is well known that the structural stability of aluminum oxide is very high, and it is very dense, which is the fundamental reason for the addition of Al and/or aluminizing to improve the corrosion resistance and high temperature resistance of the alloys [28–30].

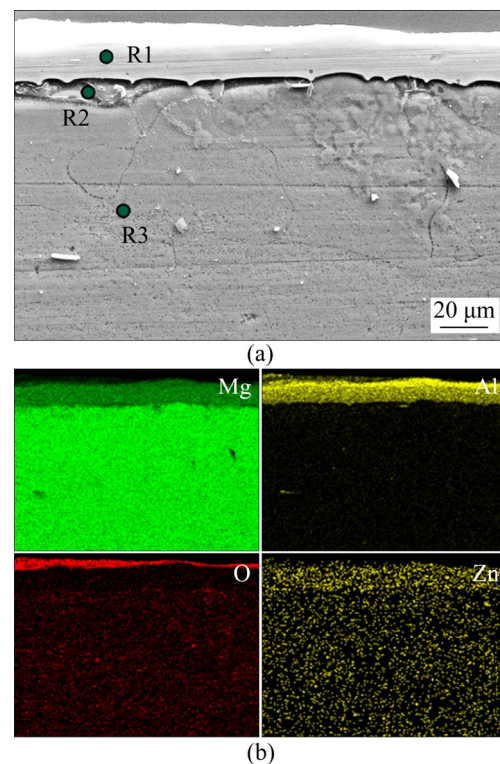


**Fig. 4** Secondary electron imaging (SEI) image (a) and EDS maps (b) of PA-2 sample

**Table 2** EDS analysis results at Points R1–R3 in Fig. 4(a)

Point	Mass fraction/%		Molar fraction/%	
	Mg	Al	Mg	Al
R1	53.18	46.82	55.76	44.24
R2	87.24	12.76	88.36	11.64
R3	97.46	2.54	97.71	2.29

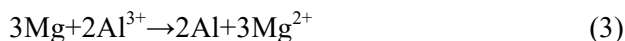
Figure 5 shows the growth mechanisms of the coatings of the two samples. For the PA-1 sample,  $\text{AlCl}_3$  will react with  $\text{NaCl}$  firstly [24,31]:



When the matrix comes into contacting with molten salt,  $\text{Mg}$  may undergo the following replacement reaction with  $\text{Al}^{3+}$  in molten salt and produce active  $\text{Al}$  atoms:



The Gibbs free energy of Reaction (2) varies as  $\Delta G = -461997 + 5.071t$  (calculated using thermodynamic data [24]). In the temperature ( $t$ ) range of this study, the  $\Delta G$  is far less than zero, which means that the reaction can occur spontaneously. By synthesizing Reactions (1) and (2), the following equivalent reaction can be obtained:



During the pack-cementation treatment, the  $\text{Al}^{3+}$  ions continue to penetrate into the  $\text{Mg}$  matrix, resulting in high  $\text{Al}$  concentration in the coating. When the  $\text{Al}$  concentration exceeds the solid solution limit in  $\text{Mg}$ , the eutectic-like structure of  $\gamma\text{-Mg}_{17}\text{Al}_{12} + \delta\text{-Mg}$  will form firstly. Subsequently, during the cooling process, the supersaturated  $\delta\text{-Mg}$  phase will precipitate the  $\text{Al}$ -rich  $\text{Mg}_{17}\text{Al}_{12}$  phase, as shown in Fig. 5(a). Since these phases are formed at low temperatures during the cooling process, their size is smaller than that of the  $\text{Mg}_{17}\text{Al}_{12}$  phase in the eutectic-like product of the diffusion reaction. Additionally, during the cooling process, the outmost layer precipitates out the  $\text{Mg}$ -rich phase of  $\text{Mg}_2\text{Al}_3$  according to the  $\text{Al}\text{-Mg}$  binary phase

diagram [22]. The melting point of the  $\text{AlCl}_3\text{-NaCl}$  system is very low ( $157^\circ\text{C}$  at equal molar fraction). The AZ31 sample originally exists in the molten salt, and the surface reacted with the salt, which can also be considered as a kind of corrosion behavior. However, as the chemical reaction occurs,  $\text{Al}$ -rich coating is formed on the surface of AZ31, which can effectively slow down the corrosion of the  $\text{Mg}$  substrate.

For the PA-2 sample, pure  $\text{Al}$  powders were added as the feedstock to the packed powders. The  $\text{Al}$  powder at  $400^\circ\text{C}$  is not activated [32], and the number of  $\text{Al}$  atoms directly diffused into the magnesium substrate is very small. Since the packaging powder and the aluminizing process are all carried out under atmospheric pressure, a small amount of oxygen is inevitable in the packed powders. As the strong oxidizing element, at high temperatures,  $\text{Al}$  atoms can react with oxygen to form alumina during the pack-cementation. Although  $\text{Al}$  ions in  $\text{AlCl}_3$  powder can still penetrate into the matrix by Reaction (3) to form the  $\text{Al}\text{-Mg}$  SS ( $\delta\text{-Mg}$ ) and  $\text{Mg}_{17}\text{Al}_{12}$  precipitate. However, the alumina layer is dense, which hinders the diffusion of  $\text{Al}$  ions into the magnesium substrate, resulting in the formation of very thin layer of the  $\gamma\text{-Mg}_{17}\text{Al}_{12} + \delta\text{-Mg}$ , as shown in Fig. 5(b). One would presume that the  $\text{Al}_2\text{O}_3$  layer may also be formed during sample preparation for the microstructure characterization, because the  $\text{Al}$ -containing coating is also exposed to oxygen during grinding and polishing. However, by comparing the distribution of  $\text{O}$  in the coatings of PA-1 (see Fig. 3) and PA-2 (see Fig. 4) samples, we can find that the  $\text{O}$  in the

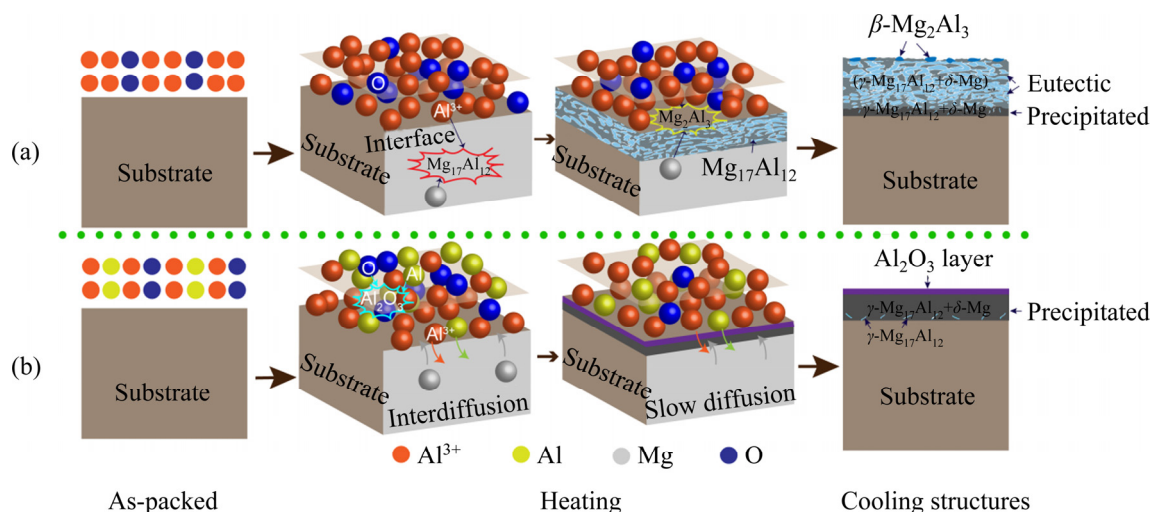


Fig. 5 Microscopic mechanism of coating formation: (a) PA-1 sample; (b) PA-2 sample

PA-1 sample is mainly enriched in the Mg-rich area, while the O content in the Al-rich area is significantly low, as shown in Fig. 3(c). Such phenomena aptly indicate that O in the coating of the PA-1 sample was introduced during the sample preparation. This is because Mg is more likely to be oxidized in an environment exposed to air and water than Al during the sample preparation [33]. On the contrary, the low O content in the Mg-rich region of the PA-2 sample just means that the  $\text{Al}_2\text{O}_3$  layer is not formed in the subsequent sample preparation for the microstructure characterization. In addition, it should be pointed out that due to the high chemical stability and high density of aluminum oxide, once the aluminum oxide layer is formed, it will seriously slow down the active Al atoms or Al ions continue to diffuse into the matrix. This is the reason why the coating thickness of the PA-2 sample is much lower than that of the PA-1 sample.

### 3.3 Properties

#### 3.3.1 Microhardness

Figure 6 shows the microhardness distributions of the various samples. Obviously, compared with the original AZ31 magnesium alloy (HV 53), the surface microhardnesses of the aluminized PA-1 and PA-2 samples are increased to HV 167 and HV 111, respectively. Moreover, compared with the uncoated sample, the microhardness of the internal matrix does not change much after surface aluminizing, and no obvious softening is found. The increase in surface hardness of the PA-1 and PA-2 samples is mainly due to the formation of eutectic-like products and the precipitation of  $\gamma\text{-Mg}_{17}\text{Al}_{12}$  phase and alumina layer during the aluminizing and cooling processes. The  $\text{Mg}_{17}\text{Al}_{12}$  is a hard and brittle phase with a microhardness of HV 220–280 [34,35], which is 3–5 times that of the Mg alloy substrate. Therefore, when the content of  $\text{Mg}_{17}\text{Al}_{12}$  phase in the coating increases, the microhardness is bound to increase significantly. It has been reported that the intermetallic compound of  $\gamma\text{-Mg}_{17}\text{Al}_{12}$  is one of the main strengthening phases of magnesium alloys, which can hinder the movement of dislocations and improve the strength and hardness of the material [36]. In addition, although alumina is harder than  $\gamma\text{-Mg}_{17}\text{Al}_{12}$ , it can be clearly seen that the surface layer of the PA-2 sample has a lower hardness than that of the PA-1

sample. This may be because the alumina layer on the surface of the PA-2 sample is too thin, and the length of the Vickers hardness indentation is greater than the thickness of the alumina layer, resulting in the microhardness of the PA-2 sample being much lower than that of pure alumina.

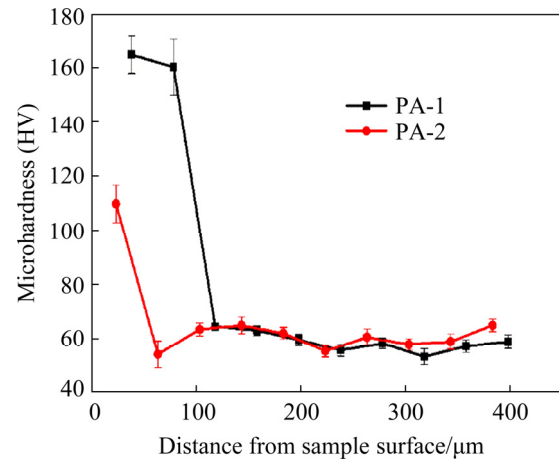


**Fig. 6** Cross-section microhardness curves of two samples

#### 3.3.2 Corrosion behavior

Figure 7 shows potentiodynamic polarization curves of various samples. All the polarization data were measured by Tafel extrapolation method, and the corrosion rate (CR,  $R_C$ ) was calculated by [16]

$$R_C = \frac{3.27 \times 10^{-3} W_e J_{\text{corr}}}{\rho}$$

where  $W_e$  is the weighted average of the ratios of relative atomic mass and valences of Mg, Al, and Zn in the sample, calculated as 12 g in this study;  $J_{\text{corr}}$  is the corrosion current density ( $\mu\text{A}/\text{cm}^2$ );  $\rho$  is the density ( $1.79 \text{ g}/\text{cm}^3$ ). The corrosion parameters are shown in Table 3. Compared with the uncoated sample, the self-corrosion potential of the PA-1 and PA-2 samples is significantly increased. The CR of the two samples is significantly reduced, while the corrosion current density is reduced by more than an order of magnitude, indicating that the corrosion resistance is improved after aluminization. Since the self-corrosion potential of the Al–Mg compounds is higher than that of Mg [20], it reduces the potential difference of the electrochemical corrosion and electromotive force of the corrosion battery. Studies have shown that the large volume fraction of  $\text{Mg}_{17}\text{Al}_{12}$  intermetallic compound ( $\gamma$ -phase) can not only increase the hardness of the alloy, but also improve the corrosion

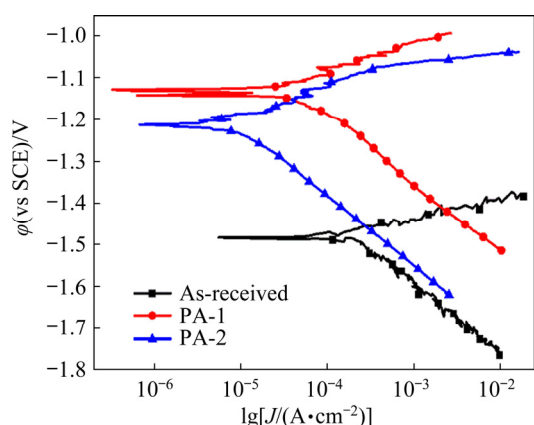


**Fig. 7** Potentiodynamic polarisation curves of different samples

**Table 3** Corrosion potential ( $\phi_{\text{corr}}$ ), corrosion current density ( $J_{\text{corr}}$ ) and average corrosion rate of samples

Sample	$\phi_{\text{corr}}$ (vs SCE)/ V	$J_{\text{corr}}$ / ( $\text{A}\cdot\text{cm}^{-2}$ )	$R_C$ / ( $\text{mm}\cdot\text{a}^{-1}$ )
As-received	-1.48	$2.91\times 10^{-4}$	6.393
PA-1	-1.13	$4.38\times 10^{-6}$	0.097
PA-2	-1.21	$1.01\times 10^{-5}$	0.223

resistance of the magnesium alloy. This is because the  $\gamma$ -phase can be used as an anode barrier to inhibit the overall corrosion of the alloy [22]. This is the main reason for the lower corrosion rate of the PA-1 sample. Although the corrosion resistance of  $\text{Al}_2\text{O}_3$  is stronger than that of any second phase in magnesium alloy, the thickness of  $\text{Al}_2\text{O}_3$  coating is too thin and not uniform enough, but it may be damaged prematurely during sample preparation and testing, resulting in the lower corrosion resistance of PA-2 sample.

The corrosion morphology of each sample after the polarization test is shown in Fig. 8. It can be clearly seen that the surface corrosion pits of the untreated sample are very large (see Figs. 8(a) and (d)), indicating that the sample has been severely corroded. The corrosion surface morphology of the PA-1 sample (see Figs. 8(b) and (e)) is much flatter than that of the as-received sample, and the corrosion pit of PA-2 sample (see Figs. 8(c) and (f)) is much smaller than that of the as-received sample, but slightly larger than PA-1 sample. This further illustrates that the Al–Mg coating can improve the corrosion resistance of AZ31 magnesium alloy, while the corrosion resistance of the PA-2 sample is slightly lower than that of the PA-1 sample. The continuous Al–Mg intermetallic compound layer can play an anti-corrosion role, thereby greatly enhancing the corrosion resistance of magnesium alloy [20].

## 4 Conclusions

(1) When  $\text{AlCl}_3$  powder is used as the activator, the coating thickness is larger than the coating using  $\text{AlCl}_3$  and pure Al composite powder as the activator, but the latter has better flatness.

(2) The coating is composed of a small amount of  $\beta\text{-Mg}_2\text{Al}_3$ , coarse eutectic-like structure of ( $\gamma\text{-Mg}_{17}\text{Al}_{12}$  +  $\delta\text{-Mg}$ ) and fine  $\gamma\text{-Mg}_{17}\text{Al}_{12}$  precipitations when using  $\text{AlCl}_3$  powder as the activator, while it only contains a thin  $\text{Al}_2\text{O}_3$  layer and a small amount of fine  $\gamma\text{-Mg}_{17}\text{Al}_{12}$  precipitations when using the mixture powders of  $\text{AlCl}_3$  and pure Al as the activator.

(3) For pack-cementation aluminizing that is

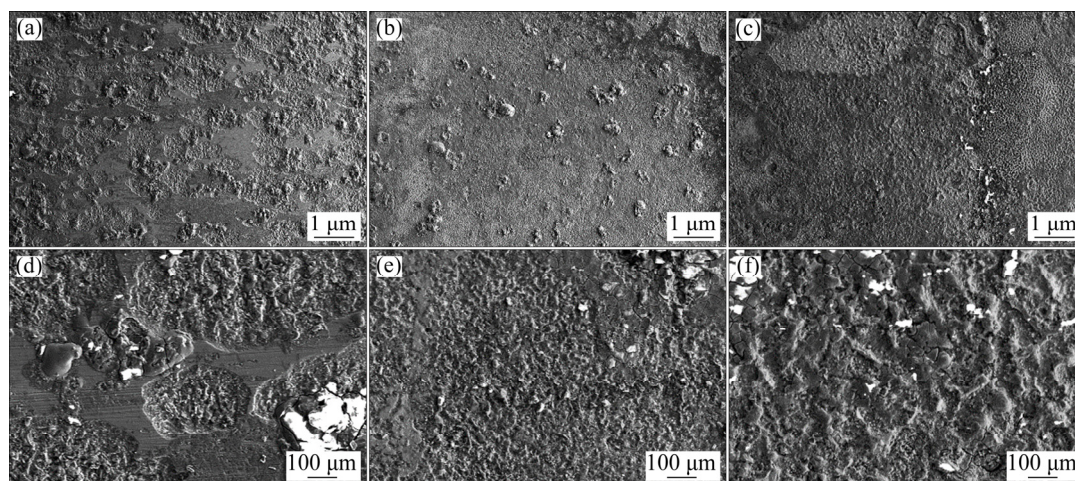


**Fig. 8** Corrosion morphologies of different samples: (a, d) As-received; (b, e) PA-1 sample; (c, f) PA-2 sample

not protected by high-vacuum or inert gas, the addition of pure Al powders can easily introduce an  $\text{Al}_2\text{O}_3$  layer into the coating to prevent active Al ions further penetrating into the magnesium matrix, resulting in a thin Al-containing coating.

(4) Both Al-containing coatings can effectively improve the surface hardness and corrosion resistance of AZ31 magnesium alloy, but the hardness and corrosion resistance of the coating with  $\text{AlCl}_3$  as pack-cementation feedstock are slightly better than those of the coating with  $\text{AlCl}_3$  and pure Al composite as pack-cementation feedstock, owing to the thicker coating of the former.

## Acknowledgments

This work was supported by the National Natural Science Foundation of China (No. 51575073), International Cooperation Special Project in Science and Technology of China (No. 2015DFR70480), and Scientific and Technological Research Program of Chongqing, China (Nos. cstc2017jcyjBX0031, cstc2018jszxcydzX0126).

## References

- [1] ZENG R C, LIU L J, PANG T T, ZHANG F, ZHANG W W, LI S Q, CUI H Z, HAN E H. Corrosion resistance of silane-modified hydroxide zinc carbonate film on AZ31 magnesium alloy [J]. *Acta Metallurgica Sinica (English Letters)*, 2015, 28(3): 373–380.
- [2] SONG B, DU Z W, GUO N, YANG Q S, WANG F, GUO S F, XIN R L. Effect of free-end torsion on microstructure and mechanical properties of AZ31 bars with square section [J]. *Journal of Materials Science and Technology*, 2021, 69: 20–31.
- [3] TEKUMALLA S, GUPTA M. An insight into ignition factors and mechanisms of magnesium based materials: A review [J]. *Materials and Design*, 2017, 113: 84–98.
- [4] GUO S F, PAN F S, ZHANG H J, ZHANG D F, WANG J F, MIAO J, SU C, ZHANG C. Fe-based amorphous coating for corrosion protection of magnesium alloy [J]. *Materials and Design*, 2016, 108: 624–631.
- [5] KALINICHENKO O O, HOLOVENKO V O, ROIENKO K V, MISNYANKIN D O, GIRIN O B, SNIZHKO L O. Corrosion of magnesium alloy AZ31 coated by plasma electrolytic oxidation [J]. *Surface Engineering and Applied Electrochemistry*, 2019, 55(5): 595–601.
- [6] LIU T T, YANG Q S, GUO N, LU Y, SONG B. Stability of twins in Mg alloys—A short review [J]. *Journal of Magnesium and Alloys*, 2020, 8(1): 66–77.
- [7] DOJA S, BICHLER L, FAN S. Corrosion behavior of AZ31 magnesium alloy in highly alkaline environment [J]. *Acta Metallurgica Sinica (English Letters)*, 2017, 30(4): 367–375.
- [8] HIRMKE J, ZHANG M X, ST JOHN D H. Influence of chemical composition of mg alloys on surface alloying by diffusion coating [J]. *Metallurgical and Materials Transactions A*, 2012, 43(5): 1621–1628.
- [9] SONG B, GUO N, LIU T T, YANG Q S. Improvement of formability and mechanical properties of magnesium alloys via pre-twinning: A review [J]. *Materials and Design*, 2014, 62(10): 352–360.
- [10] CHEN W, HUANG J M, PENG J. Characterisation of TiAlN PVD coatings on AZ31 magnesium alloy [J]. *Research on Chemical Intermediates*, 2015, 41(3): 1257–1266.
- [11] WU G S, ZENG X Q, DING W B, GUO X W, YAO S S. Characterization of ceramic PVD thin films on AZ31 magnesium alloys [J]. *Applied Surface Science*, 2006, 252(20): 7422–7429.
- [12] ZHANG Y L, CHEN F, ZHANG Y, DU C W. Influence of graphene oxide additive on the tribological and electrochemical corrosion properties of a PEO coating prepared on AZ31 magnesium alloy [J]. *Tribology International*, 2020, 146: 106135.
- [13] RAKOCH A G, MONAKHOVA E P, KHABIBULLINA Z V, SERDECHNOVA M, BLAWERT C, ZHELUDKEVICH M L, GLADKOVA A A. Plasma electrolytic oxidation of AZ31 and AZ91 magnesium alloys: Comparison of coatings formation mechanism [J]. *Journal of Magnesium and Alloys*, 2020, 8(3): 587–600.
- [14] LI M Y, HAN B, SONG L X, HE Q K. Enhanced surface layers by laser cladding and ion sulfurization processing towards improved wear-resistance and self-lubrication performances [J]. *Applied Surface Science*, 2020, 503: 144226.
- [15] PARCO M, ZHAO L D, ZWICK J, BOBZIN K, LUGSCHEIDER E. Investigation of HVOF spraying on magnesium alloys [J]. *Surface and Coatings Technology*, 2006, 201(6): 3269–3274.
- [16] HU J J, ZENG J, YANG Y, YANG X, LI H, GUO N. Microstructures and wear resistance of boron–chromium duplex-alloyed coatings prepared by a two-step pack cementation process [J]. *Coatings*, 2019, 9(9): 529.
- [17] MA Y P, LI J, ZHU J, YANG L, LIU Y G, LI Z Y, ZHAO F. Effects of treatment time on corrosion of diffusion-alloyed coatings of pure magnesium [J]. *Acta Metallurgica Sinica (English Letters)*, 2007, 20(1): 72–78.
- [18] MOLA R. The properties of Mg protected by Al- and Al/Zn-enriched layers containing intermetallic phases [J]. *Journal of Materials Research*, 2015, 30(23): 3682–3691.
- [19] LIU W X, LI X L, ZHOU X J. Formation mechanism of Al and Zn coating by solid diffusion on AZ81 magnesium alloy surface [J]. *Surface Technology*, 2018, 47(8): 36–41. (in Chinese)
- [20] ZHU L Q, SONG G L. Improved corrosion resistance of AZ91D magnesium alloy by an aluminium-alloyed coating [J]. *Surface and Coatings Technology*, 2007, 200(8): 2834–2840.
- [21] LU D Z, ZHANG Q C, WANG X T, YANG L H, MA X M, WANG W C, HUANG Y L. Intermetallic layer obtained by the compact powder diffusion alloying method on AZ91D

- magnesium alloy in air [J]. *Surface and Coatings Technology*, 2017, 309: 986–993.
- [22] LU D Z, ZHANG Q C, WANG W C, GUAN F, MA X M, YANG L H, WANG X T, HUANG Y L, HOU B R. Effect of cooling rate and the original matrix on the thermal diffusion alloyed intermetallic layer on magnesium alloys [J]. *Materials and Design*, 2017, 120: 75–82.
- [23] SUN H Q, SHI Y N, ZHANG M X, LU K. Surface alloying of an Mg alloy subjected to surface mechanical attrition treatment [J]. *Surface and Coatings Technology*, 2008, 202(16): 3947–3953.
- [24] ZHONG C, HE M F, LIU L, CHEN Y J, SHEN B, WU Y T, DENG Y D, HU W B. Formation of an aluminum-alloyed coating on AZ91D magnesium alloy in molten salts at lower temperature [J]. *Surface and Coatings Technology*, 2010, 205(7): 2412–2418.
- [25] LE J J, LIU L, LIU F, DENG Y D, ZHONG C, HU W B. Interdiffusion kinetics of the intermetallic coatings on AZ91D magnesium alloy formed in molten salts at lower temperatures [J]. *Journal of Alloys and Compounds*, 2014, 610: 173–179.
- [26] HU J J, ZHANG Y Q, YANG X, LI H, XU H B, MA C P, DONG Q S, GUO N, YAO Z W. Effect of pack-chromizing temperature on microstructure and performance of AISI 5140 steel with Cr-coatings [J]. *Surface and Coatings Technology*, 2018, 344: 656–663.
- [27] ZENG J, HU J J, YANG X, XU H B, LI H, GUO N, DONG Q S. Microstructure and formation mechanism of the Si–Cr dual-alloyed coating prepared by pack-cementation [J]. *Surface and Coatings Technology*, 2020, 399: 126142.
- [28] XU S, ZHOU Z J, LONG F, JIA H D, GUO N, YAO Z W, DAYMOND M R. Combination of back stress strengthening and Orowan strengthening in bimodal structured Fe–9Cr–Al ODS steel with high Al addition [J]. *Materials Science and Engineering A*, 2019, 739: 45–52.
- [29] XU S, ZHOU Z J, LONG F, JIA H D, GUO N, SUN Y D, YAO Z W, DAYMOND M R. Influence of Al addition strategy on the microstructure of a low-Cr oxide dispersion-strengthened ferritic steel [J]. *Advanced Engineering Materials*, 2020, 22(4): 1900879.
- [30] XU S, LONG F, PERSAUD S Y, GUO N, YAO Z W, DAYMOND M R, GAO W H, ZHANG L F, ZHOU Z J. Oxidation behavior of 9Cr–4.5Al ODS steel in 600 °C supercritical water and the effect of pre-oxidation [J]. *Corrosion Science*, 2020, 165: 108380.
- [31] HUANG W M, XIA X Y, LIU B, LIU Y, WANG H W, MAN H. Electrodeposition of aluminum on aluminum surface from molten salt [J]. *Acta Metallurgica Sinica (English Letters)*, 2011, 24(6): 443–448.
- [32] SABOORI A, CHEN X, BADINI C, FINO P, PAVESE M. Reactive spontaneous infiltration of Al-activated TiO<sub>2</sub> by molten aluminum [J]. *Transactions of Nonferrous Metals Society of China*, 2019, 29(3): 657–666.
- [33] WANG Y Q, WANG X J, WU K, WANG F H. Role of Al<sub>18</sub>B<sub>4</sub>O<sub>33</sub> whisker in MAO process of Mg matrix composite and protective properties of the oxidation coating [J]. *Journal of Materials Science and Technology*, 2013, 29(3): 267–272.
- [34] LI Y G, WEI Y H, HOU L F, GUO C L, HAN P J. Wear and electrochemical behaviour of Mg–Al intermetallic coating [J]. *Surface Engineering*, 2014, 30(12): 933–938.
- [35] ZHANG L, CAO Z Y, LIU Y B, SU G H, CHENG L R. Effect of Al content on the microstructures and mechanical properties of Mg–Al alloys [J]. *Materials Science and Engineering A*, 2009, 508(1/2): 129–133.
- [36] LIU F J, MENG Q S, LI Z S. Microstructure and properties of alloying coating on AZ31B magnesium alloy [J]. *Transactions of Nonferrous Metals Society of China*, 2016, 26(9): 2347–2354.

## AZ31 镁合金包埋渗 Al 涂层的显微组织与性能

胡建军<sup>1,2</sup>, 廖菁<sup>1</sup>, 杨显<sup>1</sup>, 曾敬<sup>1</sup>, 李晖<sup>1</sup>, 宋波<sup>3</sup>, 许洪斌<sup>2</sup>, 郭宁<sup>3</sup>, 金艳<sup>2</sup>

1. 重庆理工大学 材料科学与工程学院, 重庆 400054;

2. 汽车零部件先进制造技术教育部重点实验室, 重庆 400054; 3. 西南大学 材料与能源学院, 重庆 400715

**摘要:** 采用包埋渗法在 AZ31 镁合金表面制备 Al 涂层。利用 X 射线衍射(XRD)、背散射电子成像(BSEI)和能谱仪(EDS)等技术对 Al 涂层的物相、显微组织和成分进行表征分析。结果表明, 包埋粉的成分对涂层的物相、显微组织和厚度有显著影响。对于以 AlCl<sub>3</sub> 粉末为活化剂的样品, 涂层较厚, 涂层从表面到内部由呈梯度分布的相和组织构成, 包括少量的 $\beta$ -Mg<sub>2</sub>Al<sub>3</sub>、粗大的  $\gamma$ -Mg<sub>17</sub>Al<sub>12</sub> +  $\delta$ -Mg 类共晶结构和细小的  $\gamma$ -Mg<sub>17</sub>Al<sub>12</sub> 沉淀相。相比之下, 以 AlCl<sub>3</sub> 和纯 Al 复合粉末为活化剂的样品, 涂层相对较薄, 且含有一层薄的 Al<sub>2</sub>O<sub>3</sub> 层和少量细小的  $\gamma$ -Mg<sub>17</sub>Al<sub>12</sub> 沉淀相。这是因为对于不受高真空或惰性气体保护的包埋渗铝, 以纯铝粉为渗源材料易在涂层中引入 Al<sub>2</sub>O<sub>3</sub> 层, 从而阻碍活性 Al 离子进一步渗入到 Mg 基体中, 最终导致形成的富 Al 涂层较薄。此外, 还对两种不同铝涂层样品的显微硬度和腐蚀行为进行研究和讨论。

**关键词:** AZ31 镁合金; Al 涂层; 包埋渗; 表面渗 Al; 腐蚀性能

(Edited by Xiang-qun LI)